

## Fusion barrier distributions for heavy ion systems involving prolate and oblate target nuclei

J. D. Bierman,\* P. Chan, J. F. Liang, M. P. Kelly, A. A. Sonzogni, and R. Vandenbosch

*Nuclear Physics Laboratory, University of Washington, Seattle, Washington 98195*

(Received 7 August 1996)

Fusion excitation functions spanning the entire barrier region in 1 MeV energy steps for the two systems  $^{40}\text{Ca} + ^{192}\text{Os}$ ,  $^{194}\text{Pt}$  are presented. The results of fission fragment angular distribution measurements for fusion-fission of  $^{40}\text{Ca} + ^{197}\text{Au}$  at several projectile energies within the barrier region are also presented. The fusion data are of high enough precision to allow for extraction of the distribution of fusion barriers from the second differential of the product of  $E$  and  $\sigma$ . Basic coupled channels calculations which are in quite good agreement with the data are shown and discussed. [S0556-2813(96)04112-X]

PACS number(s): 25.70.Jj

### I. INTRODUCTION

The study of heavy ion fusion reactions has been an area of extensive work for many years [1,2]. The observation in heavy ion systems at near barrier energies of fusion cross sections several orders of magnitude greater than those expected from simple one-dimensional barrier penetration models has driven much of this work. Currently, the subbarrier fusion enhancement observed in heavy ion reactions is explained by allowing the relative motion degree of freedom to couple with internal degrees of freedom, such as static deformations [3,4], zero-point vibrational motion [5], inelastic [6] and transfer [7] channels, and also neck formation [8]. The standard theoretical calculations are performed within the coupled channels framework in which a single calculation is capable of predicting the relative cross sections for all possible reaction channels [9,10]. In a coupled channels calculation, the entrance flux is split among all possible channels, each of which confronts a different barrier resulting in a distribution of barriers to fusion rather than a single barrier. Barriers lower in energy than the one-dimensional Coulomb barrier are then responsible for the enhancement of fusion cross sections at low energies. This distribution of fusion barriers for a given system acts as a “fingerprint” of the type, relative importance, and other details of the couplings relevant to the fusion process.

A prescription was suggested [11] and later demonstrated [12] which allows for this distribution of fusion barriers to be directly extracted from the experimental measurement of the fusion cross section. The barrier distribution is acquired by twice differentiating the product of the projectile energy and the fusion excitation function  $\sigma(E)$ . The goal of this investigation was to experimentally measure the fusion excitation function for two systems which are quite similar yet should display a characteristic difference in their distributions of fusion barriers. The systems chosen for study,  $^{40}\text{Ca} + ^{192}\text{Os}$ ,  $^{194}\text{Pt}$ , are very similar except for a difference in static quadrupole deformation of the two targets. The selected isotope of osmium exhibits a prolate deformation while the isotope of platinum is oblate deformed. This shape difference is

expected to cause an observable difference in the shapes of the fusion barrier distributions for the two systems. The results of the cross section measurements and the extracted distributions of fusion barriers have been previously reported [13]. The purpose of the present paper is to furnish further details of the experimental setup, present measured fission fragment angular distributions, and also to present further coupled channel calculations for comparison with the data.

### II. EXPERIMENTAL SETUP

Because of their high  $Z^2/A$  values, any compound nuclei resulting from fusion will decay by fission. Detectors and associated electronics are required to yield both energy and relative time information to identify these fission events. Detectors for monitoring the Rutherford scattering process are also required for absolute normalization, beam position offset determination, and beam energy determination. This setup allows for fusion cross sections to be measured in relatively fine, known energy steps covering the entire barrier region. The measurements must be precise enough to allow for double differentiation to extract the barrier distributions. The following sections detail the setup used for this experiment. All experimental work was performed at the Nuclear Physics Laboratory at the University of Washington in Seattle.

#### A. Particle reactants

The  $^{40}\text{Ca}$  ions were accelerated using the Nuclear Physics Laboratory's FN Tandem Van de Graaff accelerator, which is currently capable of operating at terminal voltages up to 9 MV, in conjunction with the Superconducting Linear Accelerator. Using only the tandem accelerator,  $^{40}\text{Ca}$  beam of energies up to 120 MeV are achievable. The analyzing magnet and corresponding beam optics are able to define this energy to within  $\pm 100$  keV. The combination of accelerators is capable of producing as much as 10 particle nA of  $^{40}\text{Ca}$  beam on target with energies up to 250 MeV. At the expense of compromising intensity, higher energies may be achieved by further electron stripping before entering the linac. Using this setup, the facilities are capable of producing 0.5 particle nA of  $^{40}\text{Ca}$  beam on target with energies up to 310 MeV. The barrier region for the osmium system ranges from 180 to 230

\*Present address: Physics Department AD-51, Gonzaga University, Spokane, WA 99258-0051.

MeV and for the platinum system ranges from 190 to 240 MeV. The accelerators are capable of producing these energies without additional stripping between the tandem and linac which allows for adequate beam intensities to obtain data of sufficient statistical precision to permit determination of barrier distributions.

$^{192}\text{Os}$ , isotopically enriched to 99.0%, was acquired from Oak Ridge Isotopes. Thin targets were produced upon carbon backings at Argonne National Laboratory using this material. The osmium target thickness was  $90 \mu\text{g}/\text{cm}^2$  and the carbon backing thickness was  $35 \mu\text{g}/\text{cm}^2$ . A self-supporting  $^{194}\text{Pt}$  target made of 97.4% isotopically enriched material was acquired from Los Alamos National Laboratory. The thickness of this target was  $105 \mu\text{g}/\text{cm}^2$ . Target thicknesses of approximately  $100 \mu\text{g}/\text{cm}^2$  were important to ensure that projectile energy loss throughout the entire target was less than 1 MeV to yield good energy resolution of the data. A very thin target also ensures that no fission fragments are stopped in the target due to energy loss in the target material.

### B. Particle detectors

An  $E$ - $\Delta E$  telescope was used to detect the primary, as distinct from the complementary, fission fragment. Both the  $E$  and  $\Delta E$  parts of this assembly were silicon surface barrier detectors. The  $\Delta E$  detectors used were planar, totally depleted, silicon surface barrier detectors. These detectors had an active area of either 150 or 200  $\text{mm}^2$  and sensitive thicknesses ranging from 32 to 39 microns. The  $E$  detectors used were either totally depleted or partially depleted surface barrier detectors. Their active areas were 200  $\text{mm}^2$  and the sensitive thicknesses were all greater than 100 microns. These detectors were mounted such that the  $E$  detector was directly behind the  $\Delta E$  detector so that any particle which penetrated through the  $\Delta E$  would be detected by the  $E$  detector. An angle defining tantalum collimator was placed in front of the telescope assembly to accurately define the solid angle to which the detector was exposed. The dimensions of this collimator were determined by the constraints set by the complementary fragment detector to best insure detection of the complementary fragment for each primary fission fragment detected. To meet this requirement, a rectangular collimator 0.70 cm wide and 1.1 cm high was used. This assembly was placed approximately 10.5 cm from the target on a movable arm in the scattering chamber. The telescope was generally placed between  $34^\circ$  and  $36^\circ$  in the lab.

The primary fragments were detected at forward angles so that the complementary fragments would be detected at backward angles. As a result, the primary fragment detector encountered a relatively high flux of Rutherford scattered particles. These events were of no interest so the primary detector arrangement allowed for hardware veto of these events to lower the counting rates and strain on the electronics. To provide for this veto, the thickness of the  $\Delta E$  detector was chosen so that fission fragments, which are of higher charge and of lower energy than the Rutherford elastics, would be stopped in the detector while elastics penetrated through to the  $E$  detector. This feature allowed for the signal from the  $E$  detector to be used to veto any corresponding event in the  $\Delta E$  so that Rutherford events were never used as event triggers. This setup allowed for a 99.9% effective veto

of the elastic scattering events in the primary fragment detector.

A second detector was used to detect the complementary fragment of the fission fragment observed in the forward detector. The choice for this instrument was a seven segment, totally depleted silicon surface barrier detector. Each segment's dimensions were 0.9 cm wide by 4 cm high. The segments were separated by only 100 microns of effectively dead space. The detector then covered an active area of 6 cm wide by 4 cm high. The sensitive thickness of the detector was 300 microns, which was more than adequate to completely stop any particles of interest. The typical alpha resolution of this device was 50 keV. Each strip was biased individually, behaved and was treated as a separate detector. The strip detector was mounted in the plane defined by the primary fragment detector and the beam. The angular position was measured to within  $0.03^\circ$ . Once mounted in position, the strip detector was approximately 9 cm from the target center. Since this detector was close to the target and of such a large area, it was kept at backward angles and the primary detector was placed at forward angles. In this way, the elastic rate in the strip detector was kept relatively low to prevent complications due to high rates. The low rate was also desired to minimize accidental coincidences and minimize radiation damage to the detector.

The conversion of number of fissions detected into an absolute differential cross section required a means of relative normalization. The simplest method was to normalize to the well understood Rutherford scattering count rate. For this purpose, two monitor detectors were placed in the reaction plane at  $\pm 12^\circ$  to the beam. The detectors were mounted in holders which were affixed to the wall of the chamber and were immobile. The defining aperture for these detectors was a circular hole 5 mm in diameter. This aperture was located 63.5 cm away from the target. These detectors were either partially or totally depleted silicon surface barrier detectors. The active area was 25  $\text{mm}^2$  and the detector's sensitivity depth was 100 microns or more which easily stopped all elastically scattered beam particles. The number of elastic events detected by these monitors was used to normalize the cross section measurements. In addition, comparison of the two rates allowed for any horizontal offset of the beam position on target to be determined.

A third monitor detector was placed at  $-28^\circ$  to the beam. This detector's angle defining aperture was rectangular, 2.0 mm wide and 9.4 mm high, and was positioned 66 cm from the target position. The detector was a totally depleted surface barrier detector of active area greater than 150  $\text{mm}^2$ . The detector's sensitive thickness was 100 microns or more. This detector was used to determine the beam energy by looking at the centroid of the elastic scattering peak.

## III. DATA ANALYSIS

### A. Pre-run calibrations

A series of calibrations were performed preceding each beamtime availability. These calibrations were required to acquire information about the detector solid angles and the energy response of the detectors. Since the scattering chamber used for this experiment is shared with other experimental groups, the detector setup had to be erected before and

dismantled after each run. As a result, these basic experimental quantities were subject to change from setup to setup.

Measurements were made of the dimensions of all detector apertures and their distances from the target. These values allow for a calculation of the absolute solid angles with uncertainties depending on the measurement of the distances. Only the relative detector solid angles are required, rather than the absolute values. These relative solid angles were determined quite accurately by placing a radioactive alpha particle source at the target position and acquiring data until the desired statistics were attained. A fairly active,  $50 \mu\text{C}$ ,  $^{241}\text{Am}$  source was mounted into a standard target frame to insure proper placement at the target position. Using this source, the relative solid angles between the primary fragment detector and all three monitor detectors were easily determined. The solid angle subtended by the complementary fragment detectors were irrelevant to the determination of the differential cross sections. It was only important that this detector covered a large enough solid angle to detect all the complementary fragments.

Knowledge of the energy response of the third monitor detector was quite crucial. Since this detector's spectra was used to determine the projectile energy, it must be carefully calibrated so that the absolute energy scale was known. This calibration was performed using only the tandem accelerator which allowed for a high degree of accuracy and precision in beam energy, albeit at somewhat lower energies than those experimental data were taken with. A thin  $100 \mu\text{g}/\text{cm}^2$  natural silver target was used to minimize energy spread in the target. The target angle was chosen to minimize energy spread due to energy loss in the target. The projectile,  $^{40}\text{Ca}$ , was tuned through the tandem at the highest possible terminal voltage. The most prominent charge state was selected and focused into the scattering chamber. Data were taken until sufficient statistics had been acquired to reliably extract the centroid of the elastic scattering peak in the energy monitor detector. By taking into consideration energy loss in the target, energy loss in the detector window and the kinematics of the scattering process, the energy of the scattered particles entering the detector was determined in a straightforward manner. The extracted centroid channel number corresponded to this calculated energy. At this same terminal voltage, there were several other charge states of  $^{40}\text{Ca}$  which exited the tandem. The energy difference between these projectile charge states was quite well defined; the difference in energy between adjacent charge states was simply the terminal voltage multiplied by one unit of charge. Charge states nine, ten, eleven, and twelve were all intense enough to get sufficient beam on target to acquire data in a reasonable time. A straight line fit to these data was used as the calibration curve. The assumption was made that any pulse height defects would not significantly affect the linearity of the detector's energy response at higher energies. The calibrated energy response of the detector was then extrapolated to higher energies.

### B. Fragment detection

When acquiring actual data, any coincidence between the primary and complementary detectors represented a potential fission event. The best method of delineating fission events

from others was to construct a two-dimensional plot with the energy of the fragment in the primary detector,  $E_{\text{prim}}$ , on the vertical axis and the energy of the complementary fragment,  $E_{\text{comp}}$  on the horizontal. A separate plot was constructed for coincidences between the primary detector and each of the seven strips of the complementary detector, resulting in seven two-dimensional spectra. By forcing a similar energy response for all segments of the complementary detector, these seven plots could be summed, resulting in a two-dimensional spectrum displaying all coincident events. Figure 1 displays such a spectrum.

The fission events, as outlined in Fig. 1, are located in the center of the spectrum. The very well defined grouping of events in the upper right-hand corner with the long, vertical, downward tail is the pulser signals which are used to correct for deadtime. The same pulser signal was put into the preamps of both the primary detector and strip number seven of the complimentary detector. The amplitude of the pulser signal was chosen to significantly isolate these events from the other events of interest. A third distribution of events is located in the bottom right-hand corner and extends off the horizontal scale. This third group of events consists of deeply inelastic scattering events where the targetlike product recoils forward towards the primary detector and the projectilelike product scatters to a backward enough angle to be observed in the complementary detector. The heavy target recoil stopped in the  $\Delta E$  detector so that it could not be vetoed via electronic hardware like the elastically scattered beam.

As observed in Fig. 1, the fission events are contained in a diagonal ellipse, of sorts, with some length from the extreme points in the upper left of the spectra to the lower right and a perpendicular width. The length of this distribution is representative of the varying mass splits for the fission events. Points in the upper left corner correspond to fission events with a very asymmetric mass split, the light particle being detected in the primary detector and the heavy particle in the complementary detector. Points in the lower right part of the fission distribution are asymmetric mass splits with the heavy particle detected in the primary detector. Between these extremes lie the symmetric fission events. The width of this elliptical distribution in the perpendicular direction was determined by the spread in total kinetic energy of the fragments inherent to the fission process.

The difficulty in delineating the fission events from other coincidences is at the extremes of the distribution. The upper left corner of the fission distribution is quite well separated from other coincidences. The lower right corner, however, appears to overlap somewhat with another distribution of events. This interference is actually quite less than it appears in Fig. 1 due to the effects of summing the seven separate spectra. As a result of kinematics, these contaminating events are only observed in the most forward strips of the complementary detector. Also due to kinematics, the fission events detected in the most forward detectors correspond to asymmetric mass splits with the light particle detected in the primary detector, the upper left part of the fission distribution. There was really only one strip, strip number four, which contained both contaminant events and fission events in the lower right corner of the distribution. However, this interference affected only a very few of the total fission

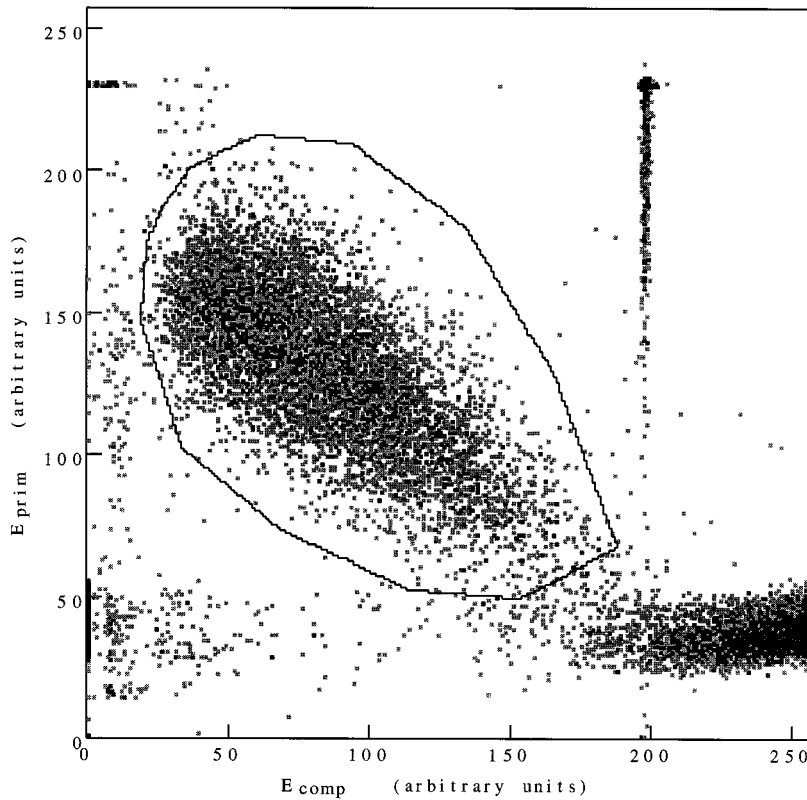


FIG. 1. Two-dimensional spectrum displaying all coincident events in the primary and complementary detectors. The vertical axis is  $E_{\text{prim}}$  and the horizontal axis is  $E_{\text{comp}}$ . This spectrum represents the sum of seven spectra correlating to the seven different segments of the complementary detector.

events. These few events were an even smaller percentage of the total fission events detected in all seven strips. As a result, by extracting the fission events from the seven separate two-dimensional plots rather than the cumulative plot, one could make a very clean delineation between the fission events and other coincidences.

An experimental concern, in addition to distinguishing fission events from other events coincident in the primary and complementary detector, was the overall efficiency for detecting the complementary fragments. Characteristics of the experimental setup designed to address this efficiency concern were the defining aperture of the primary detector, the relatively close placement of the complementary detector to the target, and the large area complementary fragment detector which was used. Due to the much larger spread of the fragment distribution in the horizontal than the vertical direction, the primary concern was of missing fission fragments horizontally in either direction. The best measure of these potentially missed events is to look at the actual distribution of the coincident fission fragment events in the seven individual strips. The number of missed events was most likely smaller than the combined total number of events in the most forward and most backward strips of the complementary detector. Figure 2 displays a histogram of this distribution. The data shown is the result of averaging over all experimental data taken for the osmium system during two weeks of beamtime. The extreme most forward and backward detectors combined accounted for approximately two percent of the total events. A negligible number of events, if any, may have missed the detector at backward angles. We estimate that less than one percent of the complementary fragments were forward or back of the strip detector. Most importantly, the efficiency of fragment detection should vary little as the projectile energy is varied over the barrier region.

### C. Beam energy determination

The energy analyzing capabilities for the final beam energy of the linac in conjunction with the tandem accelerator is only accurate to within  $\pm 1\%$ . This accuracy was by no means acceptable given this experiment's requirements and goals. The first alternative considered was to use the centroid of the elastic scattering peak in the monitor detectors at  $\pm 12$  degrees. This approach proved fruitless due to unavoidable radiation damage to these detectors resulting in a non-uniform energy response over the course of a run. The solu-

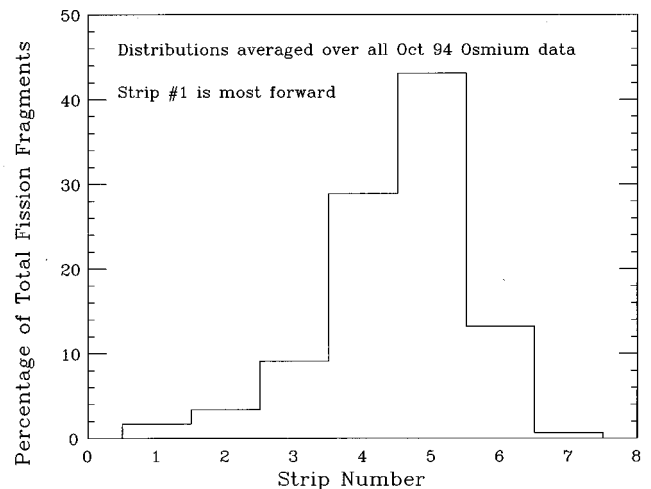


FIG. 2. Distribution of fission fragments in the complementary detector coincident with fission events in the primary detector. The seven bins correspond to the seven separate strips of the complementary detector. Fragment angle increases with increasing strip number.

tion to this dilemma was to add the third monitor detector at a more backward angle which would not be excessively radiation damaged over a multiweek period of exposure to beam. This technique appeared adequate until it was observed that for several datasets at the same beam energy the centroid appeared at a slightly lower channel number for each successive dataset. In fact, over the course of a week there seemed to be a significant shift towards lower energies. This effect was caused by carbon buildup on the front and back of the target by the beam. Once a method of accounting for this buildup was devised, the projectile energy at the target center was determined quite accurately. The fact that this technique was sensitive enough to accurately observe the buildup on the target demonstrates the care which was taken in precisely and accurately determining the different energies over the course of the experiment.

The target of interest was exposed to beam for approximately eight hours at each bombarding energy. In addition, data were taken using the thin,  $100 \mu\text{g}/\text{cm}^2$  silver target for about six minutes at each energy, three minutes at the start and three at the end. Since the silver target was exposed to beam for such a short time, a negligible amount of buildup was deposited on this target. As a result, there was no observable shift, over the course of the run, in the centroid of the elastic scattering peak associated with the silver target. These centroids were used to determine the actual bombarding energy for each data point. The centroid from the energy monitor when the target of interest was in place was used to determine the thickness of buildup which the beam traversed. This value was then used, in conjunction with the beam energy determined from the silver data, to find the projectile energy at the center of the target. The energy loss corrections were made using data taken from Ref. [14]. The carbon buildup on the osmium target ranged from an assumed initial amount of  $0.0 \mu\text{g}/\text{cm}^2$  to a final value of  $35 \mu\text{g}/\text{cm}^2$  after two weeks of beam exposure. Buildup upon the platinum target eventually reached a thickness of approximately  $40 \mu\text{g}/\text{cm}^2$  over the course of several weeks of beam exposure. The targets were chosen to be quite thin, approximately  $100 \mu\text{g}/\text{cm}^2$ , so that the range of energies at which the reaction may have occurred was relatively small, less than 1 MeV. The assumption was made that the cross section varies roughly linearly over this small range so that the measured average cross section could be associated with the projectile energy at the center of the target.

#### D. Differential cross section analysis

The next step in the analysis was to determine the differential fusion cross sections. The differential fusion cross sections were calculated using Eq. (1):

$$\frac{d\sigma}{d\Omega_{\text{fiss}}}(\theta_{\text{c.m.}}) = \frac{1}{2} \frac{N_{\text{fiss}}}{N_{\text{Ruth}}} \frac{d\sigma}{d\Omega_{\text{Ruth}}}(\theta_{\text{c.m.}}) \frac{\Delta\Omega_{\text{Mon}} J_{\text{fiss}}}{\Delta\Omega_{\text{prim}} J_{\text{Ruth}}}. \quad (1)$$

The number of fission events and the number of elastic events in the monitors were extracted from the data. The correct solid angle ratio was measured, as was the correct angular location and projectile energy. These quantities were used to calculate the Jacobians for converting to the center-of-mass frame for both the fission events and the elastic events. The elastic scattering differential cross section was

also calculated based on these angle and energy determinations. This differential cross section was associated with the determined projectile energy at the center of target and an angle  $\Theta$  computed by converting the primary fragment detector's lab angular location to the center-of-mass frame of the fission fragments. A final correction was made for any electronics or data acquisition system deadtime. This was done by determining the ratio of the number of observed pulser events in the two-dimensional spectra and the actual number of pulser events generated as counted by a scaler. This ratio describes the total deadtime in the data acquisition setup. Dividing the previously calculated differential cross section by this ratio yielded the true differential cross section.

#### IV. MEASUREMENT OF FISSION FRAGMENT ANGULAR DISTRIBUTIONS

Before the differential cross section could be converted to a total cross section, the full angular distribution of the fission fragments must be understood. To this end, two short runs were spent measuring the fission fragment angular distribution for the system  $^{40}\text{Ca} + ^{197}\text{Au}$ . A gold target was chosen because it is similar in mass to the targets of interest and would allow for preserving the fragile, thin osmium and platinum targets. Gold targets of comparable thickness were also available which makes this system quite analogous to the systems of particular interest. The previously discussed procedure and analysis were carried out to determine the differential cross section at several different angles, thus mapping out the fragment angular distribution.

Angular distributions were measured at several different energies in the barrier region and also at one energy considerably above the barrier. A transition state model calculation of the fragment angular distribution was then fitted to the experimental data. Figure 3 shows two experimental angular distributions and the respective fitted curves. Also shown in Fig. 3 are angular distributions at two different projectile energies, 247 MeV and 222 MeV, both normalized to yield the same integral when integrated over solid angle. The dotted line represents an isotropic angular distribution which has been normalized to yield also the same integral. There is very little change in the angular distribution over the barrier region. The ratio of the total cross section and the differential cross section at an angle near the point where the angular distribution intersects a similarly normalized isotropic distribution changes even less. The calculated angular distributions which best fit the experimental results were used to determine this relationship between the total cross section and the differential cross section at a certain angle. On the basis of these results, the differential cross sections were only measured at one angle, approximately  $42^\circ$  in the center-of-mass frame, at each energy for the osmium and platinum systems. This angle in the lab system was chosen because, at this angle, the ratio of the total fission cross section to the differential cross section is quite insensitive to the anisotropy. The cross section at this angle was then converted into a total cross section value using the angular distribution curves of Fig. 3. If the total cross section is plotted against  $1/E$ , a straight line may be fit to the steepest sloped region and barrier information can be extracted using the coeffi-

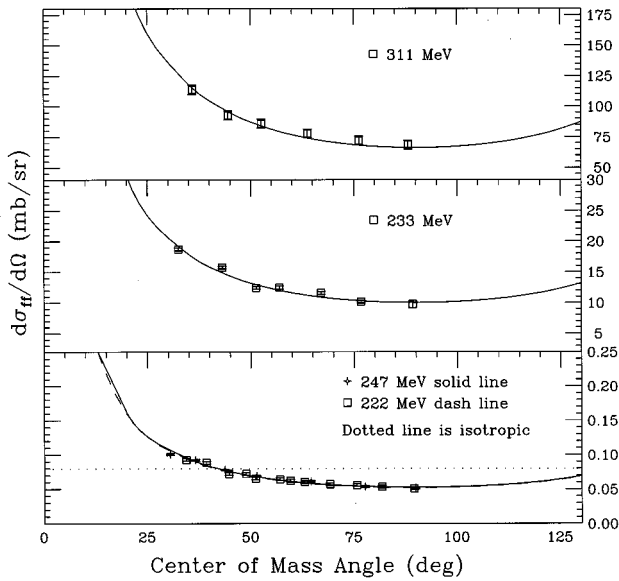


FIG. 3. Fission fragment angular distributions for the system  $^{40}\text{Ca} + ^{197}\text{Au}$  at  $E_{\text{lab}} = 311$  MeV and  $E_{\text{lab}} = 233$  MeV. The solid lines show best fit transition model calculations which are used for conversion of  $d\sigma/d\Omega$  to a total cross section. The third panel displays experimental results and corresponding best fits for the same system at  $E_{\text{lab}} = 247$  MeV and  $E_{\text{lab}} = 222$  MeV both normalized to enclose the same area. The dotted line represents a properly normalized isotropic distribution.

coefficients of the best fit line. This exercise was performed for the two targets and values of  $167.8 \pm 1.5$  MeV and  $172.1 \pm 1.5$  MeV were determined for the height of the Coulomb barrier for the Os and Pt targets, respectively. These rough estimates are in good agreement with the extracted barrier distributions shown later in Fig. 5.

## V. COMPARISON WITH CALCULATIONS

The fusion cross section measurements and extracted barrier distributions have been previously reported [13]. The results of basic coupled channels calculations, using the code CCDEF [15], were also presented to help correlate features of the experimental barrier distributions with known nuclear characteristics and couplings. The characteristic structure seen in the barrier distributions was attributed to the target nuclear deformation (quadrupole and hexadecapole), coupling to the octupole state in the projectile and coupling to a very positive  $Q$ -value transfer of two neutrons from target to projectile. While the calculations qualitatively agreed with the experimentally determined barrier distribution shapes, the calculations significantly overpredicted fusion at energies above the barrier and underpredicted fusion at energies below the barrier. The calculation also failed to reproduce the deepness of the valley between two peaks in the case of the platinum target. Further calculations have been performed to explore the cause of these discrepancies between the data and calculations.

### A. Increasing the diffuseness of the nucleus-nucleus potential

The extracted fusion barrier distributions are the best source of clues to the cause of the disagreement between data

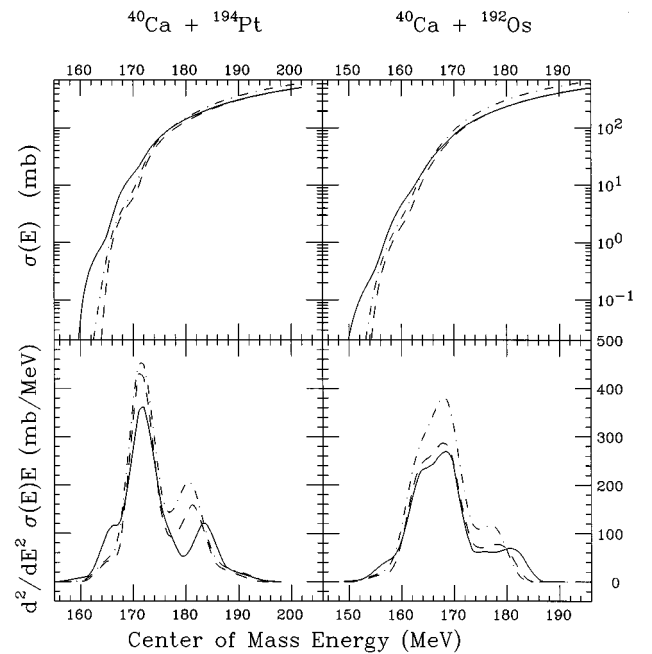


FIG. 4. Fusion excitation functions and fusion barrier distributions resulting from simple coupled channel calculations for the two systems  $^{40}\text{Ca} + ^{192}\text{Os}$ ,  $^{194}\text{Pt}$ . All three calculations include effects of target static deformation, inelastic projectile state coupling, and two neutron transfer from target to projectile ground-state coupling. For the dot-dash curve, a standard value of 0.63 fm for the nuclear diffuseness is used while the dash curve represents calculations using a value of 0.84 fm. The solid curve further includes coupling associated with the transfer of two neutrons from target to projectile resulting in an excited projectile state.

and calculations. The barrier distribution for the platinum system exhibits the most striking structure. This distribution shows two distinct peaks which are separated more clearly than the same peaks in the distribution extracted from the coupled channel calculations. This difference between the two barrier distributions implies that the barrier resolution is somewhat better in the experimental data. The resolution of the barrier distributions is reduced as a result of effects such as differentiating stepsize and quantal tunneling. While the differentiating stepsize was identical for both distributions, the smearing due to tunneling in the calculations depends on the nuclear diffuseness parameter. One would expect increasing the nuclear diffuseness to decrease the curvature of the barrier. This effect would make the barrier less penetrable, reducing the smearing of the barrier distribution due to quantum effects. The penetration for the highest partial waves will also be reduced, resulting in a lowering of the calculated fusion cross section at energies above the barrier. The decrease in barrier penetration would also be expected to reduce the fusion cross section at energies below the barrier.

Previous studies of barrier distributions [12,18,19] found increasing the nuclear diffuseness improved the agreement between simple coupled channels calculations and experimental data. If only the nuclear diffuseness is changed, the height of the barrier will also shift. Since the height of the barrier is fixed by the data, any change in the nuclear diffuseness must also be accompanied by a change in the nuclear depth or radius to retain the correct barrier height.

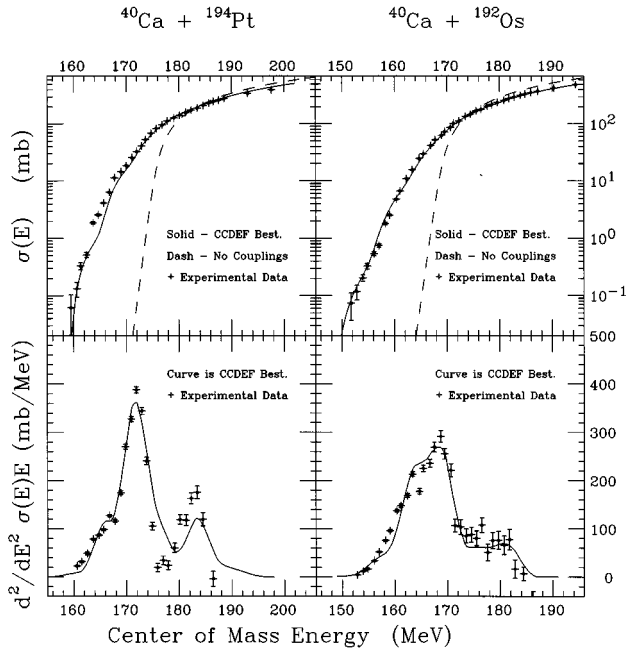


FIG. 5. The experimentally determined fusion excitation functions and fusion barrier distributions are compared with the results of coupled channel calculations including all effects described in the article. The dash fusion excitation curve represents a simple, one-dimensional barrier penetration calculation.

Figure 4 compares coupled channel calculations with the default nuclear diffuseness,  $a=0.63$  fm (dot-dash curve), and calculations with this parameter increased by 33% (dash curve). A significant reduction of the fusion cross section at energies above the barrier is apparent as is some decrease in fusion at energies below the barrier. The smearing of the barrier distribution structure is also slightly reduced, in agreement with the experimental data. This effect is most clearly demonstrated by the narrowing in the width of the main peak for each system. It should be noted that previous fits to other fusion excitation functions and barrier distributions have also indicated a larger nuclear diffuseness [19,16,17].

### B. Inclusion of additional transfer channel

While increasing the nuclear diffuseness parameter remedies some of the discrepancies between the data and calculations, the calculations still clearly underestimate the fusion enhancement at energies below the barrier. The significant contribution to the most subbarrier fusion enhancement was from inclusion of coupling to the quite positive  $Q$ -value transfer of two neutrons from target to projectile. The  $Q$

value of this reaction channel is greater than +5 MeV for both systems. The flux of barriers at the lowest energies in the calculations were correlated to coupling with these positive  $Q$ -value channels. The further inclusion of other positive  $Q$ -value channels would be expected to account for part of the discrepancy between the calculations and data.

The transfer of two neutrons from target to projectile resulting in an excited projectile state, rather than the ground state, may be expected to be of comparable, if not larger, coupling strength. This channel would also have a quite positive  $Q$  value, although somewhat less positive than the transfer populating the ground state. Figure 4 also displays the results of calculations considering both the increased nuclear diffuseness parameter and the inclusion of coupling with the two neutron transfer to an excited state channel with a coupling strength comparable to that used for the transfer to ground-state channel, 2 MeV. The calculated fusion cross section at energies above the barrier is not significantly affected. The fusion cross section at energies below the barrier, however, is dramatically affected as further enhancement of up to several orders of magnitude is observed. The flux of low energy barriers is seen to increase for both systems.

### C. Final comparison between coupled channel calculations and data

Increasing the nuclear diffuseness parameter and including the effect of coupling to two neutron transfer to the projectile first excited state has drastically improved the overall agreement between the calculations and the experimental data. Figure 5 compares calculations with the fusion cross section data and the extracted barrier distributions for both systems. The calculations consider static deformation of the target shape (quadrupole and hexadecapole), coupling to the excited octupole state of the projectile, coupling to the transfer of two neutrons from the target to projectile resulting in the projectile ground state, and also two neutron transfer resulting in the first excited state in the projectile. These calculations are performed using a nuclear diffuseness parameter of 0.84 fm, about 33% above the default value. Identical transfer coupling strengths have been used for each system in the calculations. A  $\beta_3$  value of 0.225 has been used for the octupole state in the calcium projectile. A coupling strength of 1.8 MeV for the two neutron to ground-state transfer channel has been used for both systems. A strength of 2.2 MeV was used for the two neutron transfer to excited state channel. Table I summarizes the parameters used for the coupled channel calculations as well as literature values [20,21] of the deformation parameters for both systems. The calculations are in qualitative agreement with the data over the entire range of measured fusion cross sections. The ex-

TABLE I. Transfer channel  $Q$  values, transfer channel strengths, and deformation parameters used in coupled channel calculations for the systems  $^{40}\text{Ca} + ^{192}\text{Os}$ ,  $^{40}\text{Ca} + ^{194}\text{Pt}$ . Literature values for the deformation parameters are listed in parentheses. In addition, a  $\beta(3)$  value of 0.225 was used for the octupole state in the calcium projectile.

Nucl.	$\beta_2$	$\beta_4$	$2n$ $Q$ (MeV)	$2n$ $F$ (MeV)	$2n^*$ $Q$ (MeV)	$2n^*$ $F$ (MeV)
$^{192}\text{Os}$	0.145 (0.167)	-0.01 (-0.043)	6.52	1.8	4.99	2.2
$^{194}\text{Pt}$	-0.150 (-0.154)	-0.039 (-0.045)	5.21	1.8	3.68	2.2

tracted fusion barrier distributions also agree quite well with regard to both shape and amplitude. While the agreement of the calculations may be improved slightly by further fitting exercises, the predominant features observed in the barrier distributions and measured fusion cross sections have been well accounted for within the simple coupled channels framework assuming a constant coupling strength.

A question which we have not rigorously addressed is the possible effect of triaxiality and  $\gamma$ -soft vibrations of the target nuclei for the systems of this study. The targets are in the shape transition region, a region in which the degree and effects of  $\gamma$ -soft vibrations and triaxiality have been explored. Baktash *et al.* [22] have concluded that  $\gamma$ -soft models have better or equal success compared to rigid triaxial models in explaining their data for these transitional nuclei. The platinum system is more likely to exhibit any signature of these effects. Some work is being done [23] to modify the simple coupled channels code used for comparison with the results of our study to include these possible gamma degree of freedom effects. Preliminary results seem to indicate that inclusion of such effects may tend to "fill in" the valley even more between the two peaks in the barrier distribution for the platinum system which would not improve the agreement between calculations and data. Further work on the coupled channel code will allow for a more detailed investigation of this question. It would also be of interest to use a less simplified coupled channels code to see the effects of treating dynamical effects more exactly.

## VI. SUMMARY

An experiment to accurately and precisely determine the fusion excitation functions for the systems  $^{40}\text{Ca} + ^{192}\text{Os}$ ,  $^{194}\text{Pt}$  has been designed and completed. A method of reliably determining the projectile beam energy has also been devised and shown to work. Fission fragment angular distributions for a similar system,  $^{40}\text{Ca} + ^{197}\text{Au}$ , have been measured at several energies in the barrier region. These measurements have aided in the conversion of the differential fusion cross section measurement at a single angle into a total fusion cross section value. The resulting fusion excitation functions for the two systems of interest have been used to extract the distribution of fusion barriers which have yielded significant information about the coupling processes involved in the fusion of the nuclei. A quite simple coupled channel code has been used to perform calculations which are compared with the experimental results. The calculations and data compare quite well over the entire region of measurement for both systems with regard to both fusion excitation functions and distributions of fusion barrier.

## ACKNOWLEDGMENTS

This work was supported in part by the U.S. Department of Energy. The authors would also like to thank the Linac staff for much help with accelerator operations. Thanks also to Judith Gursky of the Los Alamos National Laboratory and John Greene of Argonne National Laboratory for preparing the targets used in this experiment.

- 
- [1] S.G. Steadman and M.J. Rhoades-Brown, *Annu. Rev. Nucl. Part. Sci.* **36**, 649 (1986).
  - [2] M. Beckerman, *Phys. Rep.* **129**, 145 (1985).
  - [3] C.Y. Wong, *Phys. Rev. Lett.* **31**, 766 (1973).
  - [4] R.G. Stokstad, Y. Eisen, S. Kaplanis, D. Pelte, U. Smilansky, and I. Tserruya, *Phys. Rev. C* **21**, 2427 (1980).
  - [5] H. Esbensen, *Nucl. Phys.* **A352**, 147 (1981).
  - [6] C.H. Dasso, S. Landowne, and A. Winther, *Nucl. Phys.* **A405**, 381 (1983).
  - [7] R.A. Broglia, C.H. Dasso, S. Landowne, and G. Pollarolo, *Phys. Lett.* **133B**, 34 (1983).
  - [8] H.J. Krappe, K. Moehring, M.C. Nemes, and H. Rossner, *Z. Phys. A* **314**, 23 (1983).
  - [9] W. Reisdorf, *J. Phys. G* **20**, 1297 (1994).
  - [10] T. Izumoto, T. Udagawa, and B.T. Kim, *Phys. Rev. C* **51**, 761 (1995).
  - [11] N. Rowley, G.R. Satchler, and P.H. Stelson, *Phys. Lett. B* **254**, 25 (1991).
  - [12] J.X. Wei, J.R. Leigh, D.J. Hinde, J.O. Newton, R.C. Lemmon, S. Elfstrom, J.X. Chen, and N. Rowley, *Phys. Rev. Lett.* **67**, 3368 (1991).
  - [13] J.D. Bierman, P. Chan, J.F. Liang, M.P. Kelly, A.A. Sonzogni, and R. Vandenbosch, *Phys. Rev. Lett.* **76**, 1587 (1996).
  - [14] L.C. Northcliffe and R.F. Schilling, *Nucl. Data Tables* **7**, 233 (1970).
  - [15] J. Fernandez-Niello, C.H. Dasso, and S. Landowne, *Comput. Phys. Commun.* **54**, 409 (1989).
  - [16] C. R. Morton *et al.*, *Phys. Rev. Lett.* **72**, 4074 (1994).
  - [17] J.R. Leigh *et al.*, *Phys. Rev. C* **52**, 3151 (1995).
  - [18] N. Rowley and M. Dasgupta, in *Proceedings of the International Workshop on Heavy-Ion Reactions with Neutron-rich Beams, RIKEN, 1993*, edited by M. Ishihara, N. Takigawa, and S. Yamaji (World Scientific, Singapore, 1993), p. 232.
  - [19] R.C. Lemmon, J.R. Leigh, J.X. Wei, C.R. Morton, D.J. Hinde, J.O. Newton, J.C. Mein, M. Dasgupta, and N. Rowley, *Phys. Lett. B* **316**, 32 (1993).
  - [20] P.T. Deason, C.H. King, R.M. Ronningen, T.L. Khoo, F.M. Bernthal, and J.A. Nolen, Jr., *Phys. Rev. C* **23**, 1414 (1981).
  - [21] F. Todd Baker, A. Sethl, V. Penumetcha, G.T. Every, W.P. Jones, M.A. Grimm, and M.L. Whiten, *Nucl. Phys.* **A501**, 546 (1989).
  - [22] C. Baktash, J.X. Saladin, J.J. O'Brien, and J.G. Alessi, *Phys. Rev. C*, **22**, 2383 (1980).
  - [23] J. Fernandez-Niello and C. Dasso (private communication).